First Investigations on the Energy Deposited in a D0 early separation scheme Dipole for the LHC upgrade

Christine Hoa / AT-MCS

Summary

This note gives the first results of energy deposition calculation on a simplified model for an early scheme separation dipole D0, located at 3.5 m from the IP. The Monte Carlo code FLUKA version 2006.3 has been used for modelling the multi-particle interactions and energy transport. After a short introduction to particle interaction with matter and power deposition processes, the FLUKA modelling is described with bench marked power deposition calculation on the TAS, the absorber located in front of the triplet quadrupoles. The power deposition results for the D0 early scheme are then discussed in details, with the averaged and peak power density, and the variations of the total heat load in the dipole with the longitudinal position and with the aperture diameter.

1   Introduction

In a first study [2], we investigated the energy impinging on the dipole of an early separation scheme and its parametric dependence. Only a fraction of this incident energy is actually absorbed and converted into heat. In this second study, we concentrate on a first evaluation of the heat to be removed and its parametric dependence. The early separation scheme [1] requires indeed a small dipole positioned deeply inside the LHC experimental detectors. Likewise, a significant luminosity upgrade benefits from a reduced distance between the IP and the triplets [1]. Given the much increased luminosity and the reduced distance to the IP, a critical issue, in both cases, is the potential large increase of the energy and dose received by the magnets. This study considers a simplified model of dipole. The collision as well is simplified, assuming a point like co-linear collision. It is believed that this simplified model still retains the essentials of the physics involved. The power deposition is evaluated in terms of total heat load and peak power density, with longitudinal distribution along the dipole. These results shed light on the relevant parameters to take into account at magnet design stage for the feasibility of an early separation dipole.

2   Particle interactions with matter

2.1   Source particle and secondaries

The proton-proton collisions (p-p collisions) have been generated with the event generator DPMJET III. A fine characterisation of the impinging energy in the region close to the IP can be found in [2]. We recall here the relevant elements for understanding the

interactions of the particles inside the dipole. After the p-p collisions, the debris consist mostly of protons, charged and neutral pions, neutrons, photons, electrons and positrons (see Figure 1) [2]. It has to be noted that the charged and neutral pions represent a great part of the secondary particles in terms of mean number, but also in terms of energy. The neutral pions or pionzeros have a short life time and decay just after the collision into 2 photons. The particle families that impinge the dipole at 3.5 m from the IP are then: photons, protons, charged pions and neutrons. The energy range of the secondary particles spans mainly from 1 GeV to 1000 GeV. The following section gives the energy loss processes by type of secondary particles.
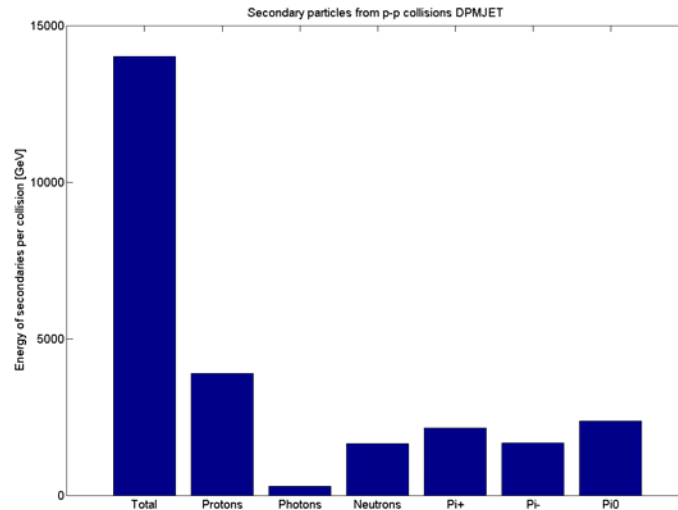

Figure 1: Histogram of energy of secondary particles/ p-p collision

2.1 Mechanisms for energy losses in matter

Charged particles, photons and neutrons interact with matter and loose energy according to statistical processes. The main interaction processes of particles with matter are recalled in this section but detailed descriptions can be found in a broad literature on the topic of particle interaction with matter [6-9].

2.1.1 Charged particles (protons, charged pions, electrons)
Charged particles interact electromagnetically with atomic electrons in the material. The energy losses of charged particles are made up mostly of 2 components:

- The energy losses due to the interactions with atomic electrons (collision stopping power). They are called the **multi-scattering Coulomb interaction**s and often lead to ionization of the atoms in the matter.

- The energy losses due to **Bremsstrhahung interactions** (radiation stopping power). An electromagnetic radiation is produced by the deceleration of the particle, when deflected by another charged particle, such as an atomic nucleus.

2.1.2 Photons

The photons interactions with matter can consist of 3 main processes:

- **Pair production** is the major process at high energies: photons interact with atomic nucleus and produce a pair of electron and positron.

- **Compton scattering** is dominant in the range of 0.1 and 10 MeV: photons are scattered with a decrease in energy after an interaction with an atomic electron.

- **Photo-electric effect** at low energies: an electron is ejected and a photon is absorbed.

2.1.3 Neutrons

Since they are non charged, the neutrons interact with the matter via the strong nuclear force which has a short range, so the interactions with nuclei occur less and the neutrons are penetrating the matter. At high energy, the energy losses are due to elastic and inelastic scattering interactions. Neutrons can produce hadronic showers.

2.2 Electromagnetic showers

The collision debris at high energy generate electromagnetic showers. High energetic electrons and photons interact with matter mainly through Bremsstrahlung and pair production, respectively. Photons and e+ and e- pairs are produced, which in turn interact, thus producing a cascade of particles. The products of the interactions have lower energy than the incoming particles. The growth of the cascade will stop when the energies of the particles fall below the domain where radiation losses are dominant. The remaining particles dissipate their energy through ionization. The low energy photons in the tail of the shower dissipate their energy through Compton scattering and photo-effect.

To describe an electromagnetic cascade, the main parameters are:

- The **radiation length**: it gives the longitudinal development of the shower for high energy electrons.

- The **critical energy**: the energy at which radiation losses balance collision losses.

- The **attenuation length** [5] of a photon is the distance τ into the material when the probability P has dropped to 1/e that the photon has not been absorbed.

$$P(x) = e^{-x/\tau} \tag{1}$$

- For a charged particle passing trough matter, its energy decays exponentially due to ionization until it becomes zero. The **stopping power (S)** is the averaged energy loss of the particle per unit path length. This parameter depends on the type and energy of particle and the properties of the material. The **range (R)** of a charged particle is considered as the average distance along the path travelled by the particle until it comes to rest.

$$S = -\frac{dE}{dx} \tag{2}$$

$$R = -\int_{E_0}^{0} \frac{dE}{-\left(\dfrac{dE}{dx}\right)} \tag{3}$$

Figure 2 shows the stopping power and range of electrons with kinetic energy from 10^{-2} to 100 MeV in Copper, with the contribution of the radiation and collision energy losses [6]. At high energy range, the radiation power takes over the collision power.
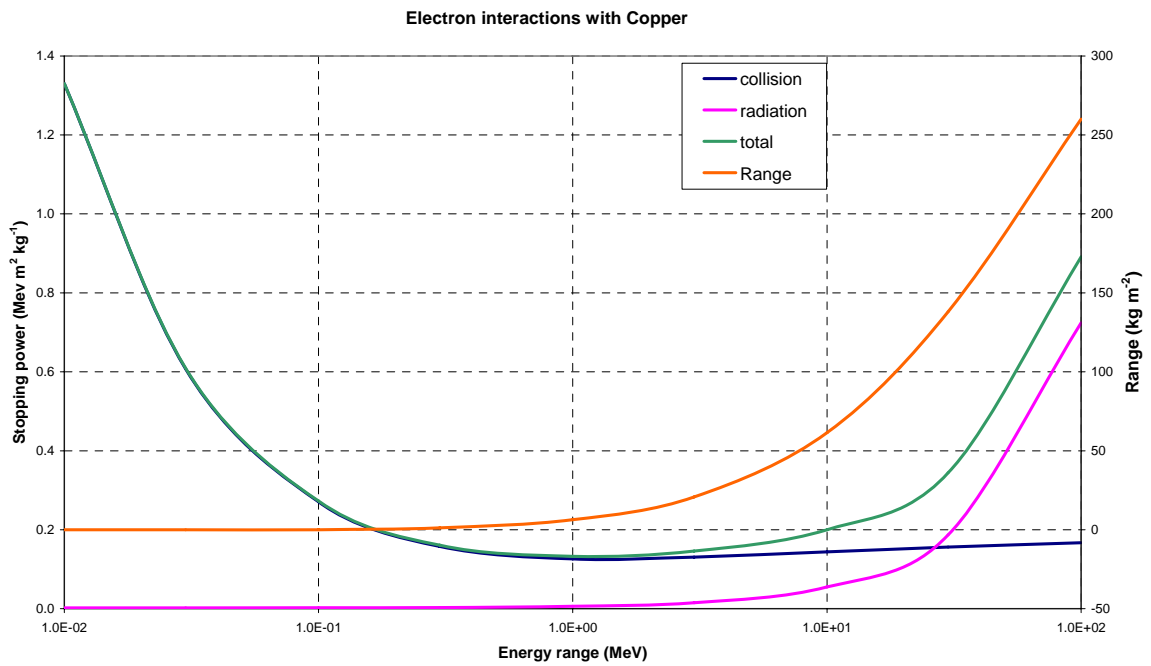

Figure 2: Electron interaction in Copper [10]

Among the products of the p-p collisions, the photons are mostly energetic particles in the range of 1 GeV to 1000 GeV [1]. The energetic photons will interact with copper in pair production events and the attenuation length in this range of energy is around 20 mm (Figure 3) [7].
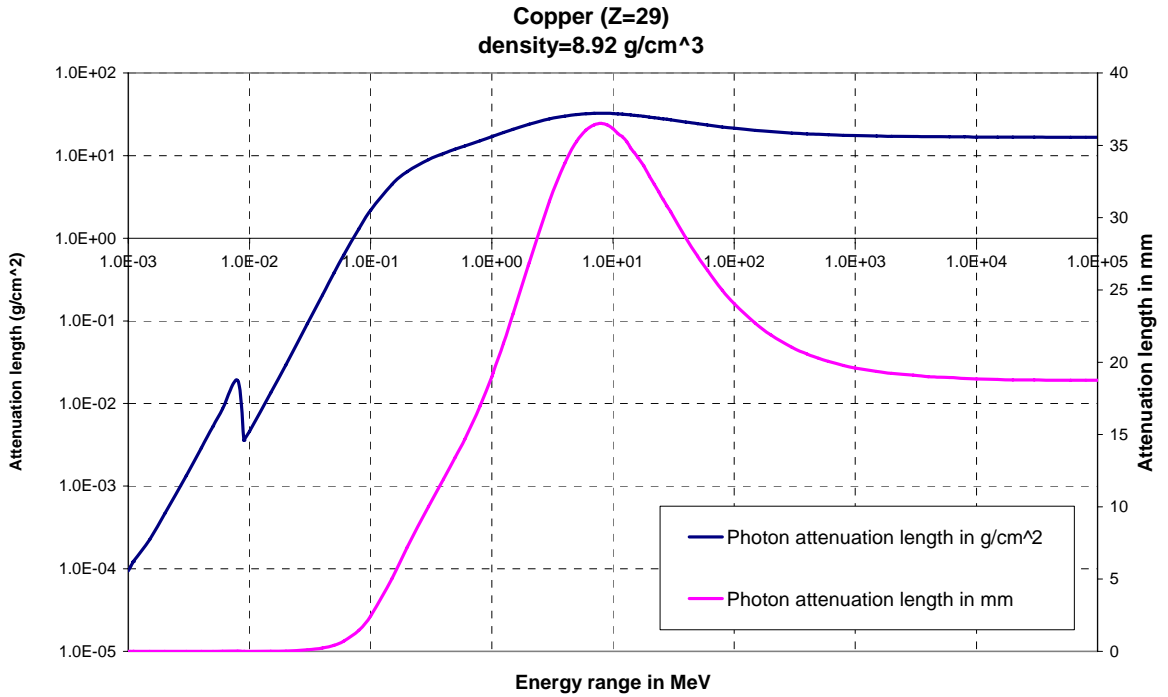
Figure 3: Attenuation length for photons in Copper [11]

2.3   Hadronic showers

A hadronic shower can be produced by a high energy hadron, such as a charged pion. It interacts with the atomic electrons to produce partially electromagnetic showers, but also can interact with nuclei via the strong nuclear force and produce secondary hadrons. Unlike the electromagnetic shower that produces pairs, the strong interaction allows any number of hadrons to be created. The average multiplicity is energy dependent. In the FLUKA implementation of hadron-nucleus interactions several lower energy hadrons can be produced. The models are described in [13].

In the case of interactions with copper, the ranges of different particles have been found in the literature ([10-11]). For energy of 100 MeV, protons, pions, muons and electrons have ranges in Copper of 11 to 50 mm.

100 MeV Particles	Range in (kg.m^{-2})	Range in mm
Protons	117	13.1
Pions	395	44
Muons	446	50
Electrons	260	29

Table I: Range of particles of 100 MeV [10]

3 Calculation strategy and validation

3.1 Beam Parameters

In this note, the events are assumed head on (no crossing angle), point like bunches collisions at the interaction point (IP). The parameters are given in Table II. The total cross section is assumed to be 80 mbarn (20 mbarn are single diffractive events and 60 mbarn are inelastic non diffractive events). The elastic scattering (40 mbarn) has been neglected as the scattered protons do not interact with the insertion region elements but, after several revolutions, they would be absorbed by the collimator systems.

p-p collisions	Beam parameters
Px, Py (TeV)	0
Pz (TeV)	+7/-7
σx, σy, σz (m)	0
L, Luminosity ($cm^{-2}s^{-1}$)	10^{35}
A, Cross section (mbarn)	80

Table II : Beam parameters

3.2 Computing parameters

For the tracking and energy transport, the cut off parameters are given in Table III. They are very conservative values and lead to a complete tracking of the electromagnetic cascades in the material. The two cut offs for neutrons correspond to two different processing by FLUKA, depending on the energy range.

Number of primary particles	3 runs of 2000
Cut off energy for photons	3 keV in the dipole and beam pipe
Cut off energy for e-/+e-	30 keV in the dipole and beam pipe
Cut off energy for Muons	100 keV
Cut off energy for Hadrons	100 keV
Cut off for high energy neutrons	19.6 MeV
Cut off for low energy neutrons	1E-14 GeV 72 neutron energy groups down to thermal energies

Table III: FLUKA computing parameters

3.3 Conversion to deposited power

FLUKA gives the power deposition results in GeV/collision in the dipole region. The following formula (4) gives the transformation in Watts, taking into account the interaction rate at the upgrade luminosity, L=10^{35} $cm^{-2}s^{-1}$, and assuming a cross section of A= 80 mbarn.

$$Power(W) = Energy(eV) * 1.602 * 10^{-19} * L(cm^{-2}s^{-1}) * A(barn) * 10^{-24}$$

(4)

3.4 Validation: TAS modelling with FLUKA

For the purpose of validation, the energy deposited in the baseline TAS is computed and compared to results obtained by other authors. The TAS has been modelled with the characteristics found in [3] and given in Figure 4. The total length is 1.8 m and the inner aperture radius is 1.7 cm. The outer radius is 25 cm. The material is copper. It is positioned at 19.45 m from the IP.
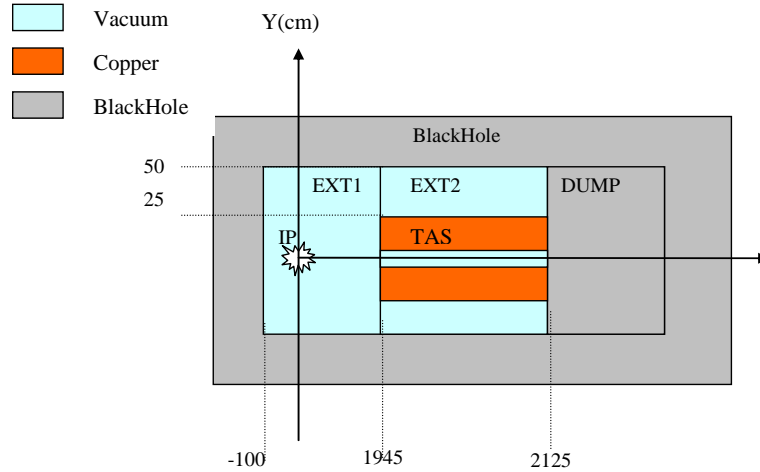

Figure 4: TAS modelling description

FLUKA computes a power deposition of 186 W with a statistical error of 2.2% for the TAS absorber, with the nominal luminosity of 10^{34} cm^{-2}s^{-1} .This result is well in line with the reference value found in [3], 184 W obtained with another Monte Carlo transport code (MARS). This result shows a 22% discrepancy with another value found in [5], 140 W, but in this case, we know that the geometry of the TAS slightly differs and the source implementation is also different. In the present calculation, the secondary source particles are generated calling on-line the DPMJET III event generator.

The power deposition in the TAS evaluated with FLUKA is thus satisfying and validates the FLUKA model for a simple geometry and a model of the beam-beam interaction.

4 D0 early separation scheme dipole

4.1 Geometrical Configuration

The entry face of the D0 dipole is located at 3.5 m from the IP. A simple copper hollow cylinder models the coils of the magnets. The thickness of the coils is 15 mm with an inner radius of 35 mm. The length of the dipole is 100 cm (Figure 5).
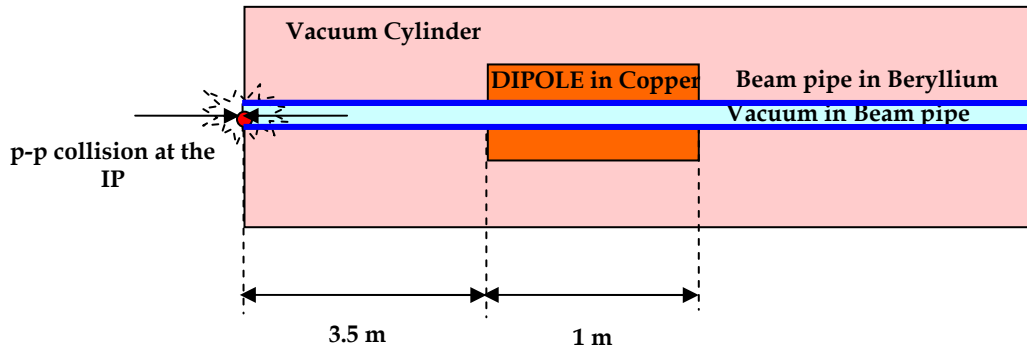
Figure 5: FLUKA modelling of D0

4.2   Magnetic field

A constant magnetic field of B_x=6 T has been assumed in the copper region and in the magnet aperture.

4.3   Meshing

The scoring binning is a cartesian mesh with the bin sizes given in Table IV. The x and y sizes correspond to the minimum dimension of a superconducting cable: the thickness of the cable is in the order of millimetre. The high longitudinal heat conduction in the cable enables to choose a large bin size in z direction, as the heat would be well evacuated.

	Min (cm)	Max (cm)	Number of bins	Bin size (cm)
x	**-5**	**5**	**50**	**0.2**
y	**-5**	**5**	**50**	**0.2**
z	**350**	**450**	**50**	**2**

Table IV: Scoring binning sizes

4.4   Power deposition results
4.4.1   Average and Maximum Power

The total power deposition (Table V) is **74.7 W** (without the magnetic field), with an average heat density of 18.8 mW/cm^3. The maximum heat density locally reaches about 95 mW/cm^3, and is even more critical with a magnetic field (117 mW/cm^3). These maximum values of heat density rise well above both the quench limits for the present Nb-Ti and Nb$_3$Sn technologies [2].

These results show that steps must be taken to reduce the heat load by a factor 8 to have a power density below the quench limit of Nb-Ti. A safety margin of 3 is required in addition at design stage to cover uncertainties on the empirical value of quench limits and the uncertainties of FLUKA modelling (geometry, materials). For peak density values, the uncertainties (FLUKA physics) imply a supplementary factor of at least 2 to get values with reasonable margin.

Taking into account these considerations, the averaged values are high but not too critical. The maximum values are very high and would be reduced with a better repartition of the energy losses, completed by a shielding, well designed to reduce the local peaks.

The power deposition in the dipole itself seems not very sensitive to its magnetic field. This result should be confirmed by further investigation: the coupled effect of a crossing angle on the beams and the magnetic field of the dipole should be characterized.

Magnetic field	Total heat deposition (W)	Average heat deposition density (mW/cm3)	Maximum heat deposition density (mW/cm3)	Quench limit Nb-Ti quads (mW/cm3)	Quench limit Nb$_3$Sn quads (mW/cm3)
No magnetic field	**74.7**	**18.8**	**95.1**	**12 [2]**	**36 [2]**
B$_x$=6 T	**69.2**	**17.3**	**116.8**		

Table V: Power deposition in D0 dipole

4.4.2   *Detailed power deposition distributions*

Figure 6 shows the spatial repartition of the power deposition in the different region of the model. 46.9% of the power is escaping through the magnet gap (8447 W). This result is in line with the analyses found in [1] and confirms that the most energetic particles are distributed in the very forward direction. The power deposition in the dipole represents only 4.2 % of the total power. The beam pipe is very thin and only 1.5 W is deposited by the debris. The remaining power is dumped in surrounding blackhole regions: it concerns mostly half of the particles coming out of the collisions going towards the left side of the IP. The blackhole regions also contain the particles of the right side of the IP that have escaped the system going through the beam pipe and the dipole.
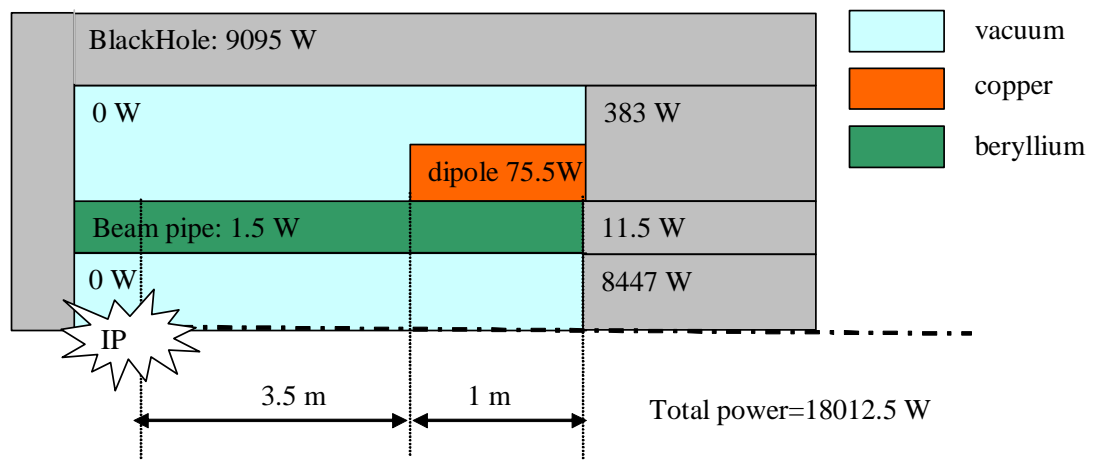

Figure 6: Power deposition distribution

MAP of power deposition in the cross section averaged for z=[350,450] without B [mW/cm³]

MAP of power deposition in the longitudinal direction average for x [-5,+5] without B [mW/cm³]
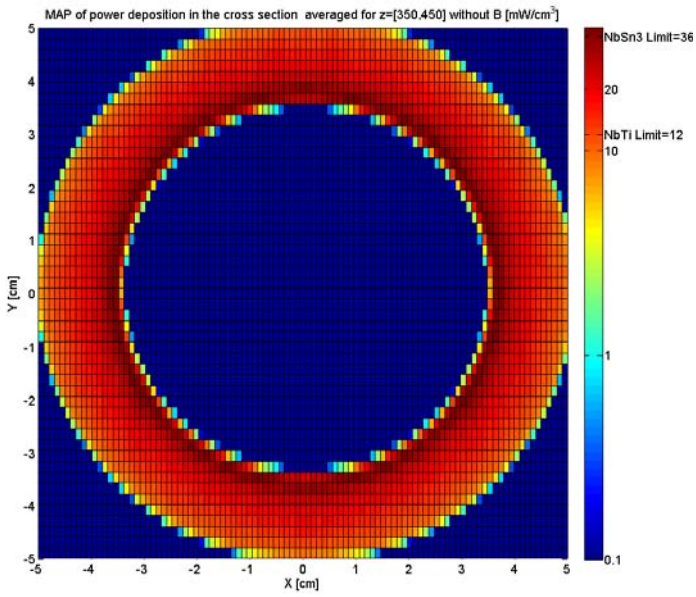
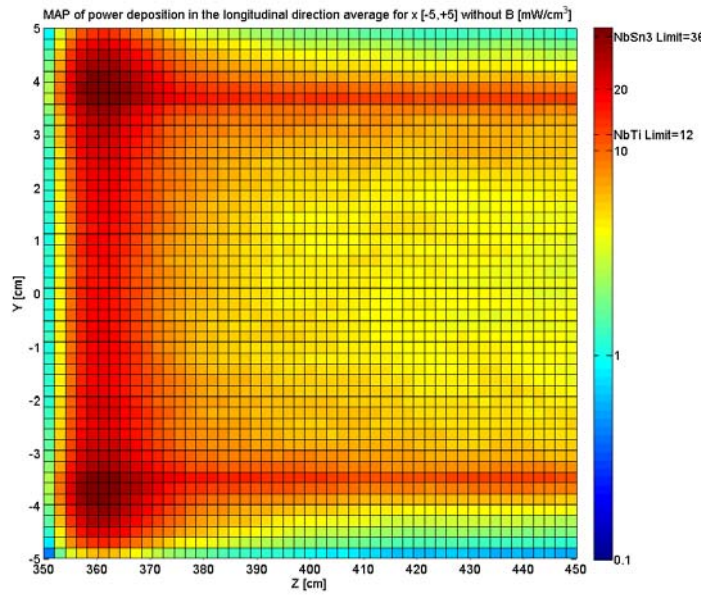Figure 7: Power deposition in D0: radial distribution (without magnetic field), averaged on total length.

Figure 8: Power deposition: longitudinal distribution (without magnetic field), averaged on X [+5,-5] cm.
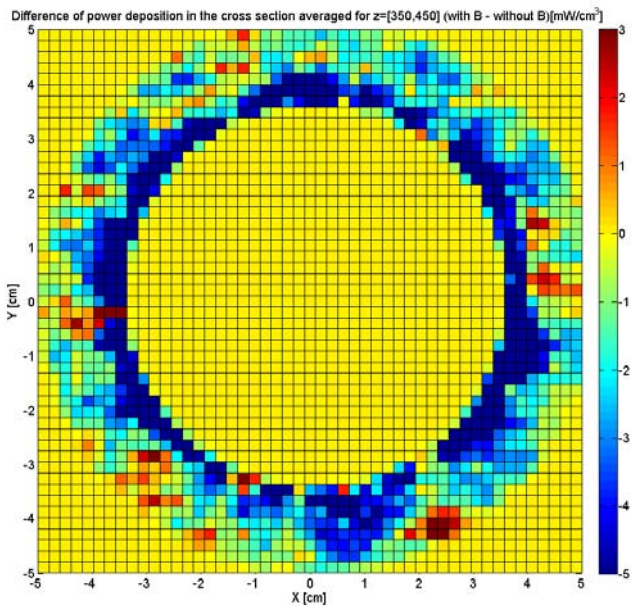

Difference of power deposition in the cross section averaged for z=[350,450] (with B - without B)[mW/cm³]

Difference of power deposition in the longitudinal direction average for x [-5,+5] (with B - without B)[mW/cm³]

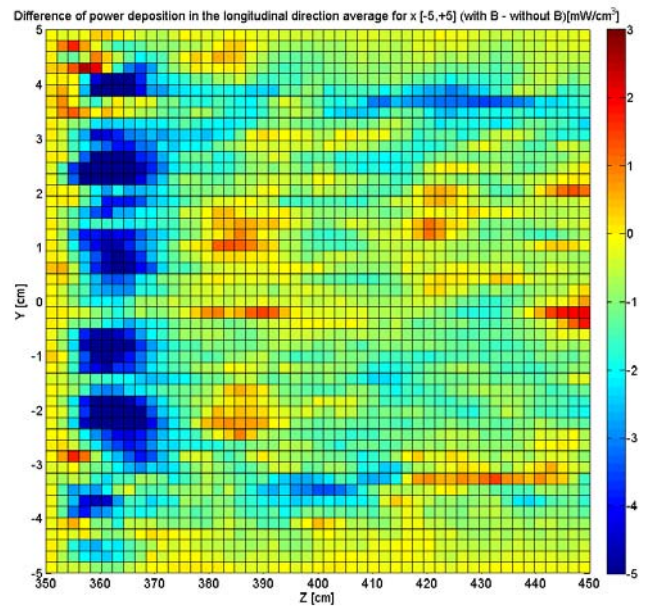Figure 9: Power deposition in D0: radial distribution Difference (with B_x-without B_x), averaged on total length.

Figure 10: Power deposition: longitudinal distribution Difference (with B_x-without B_x), averaged on X [+5,-5] cm.

4.4.3 Contour plotting: radial and longitudinal distributions

The distributions of the power deposition in the dipole, with and without the effect of a dipole magnetic field of B_x=6 T have been compared. The power deposition is uniformly distributed in the azimuthal direction (Figure 7). The highest values are located close to the beam pipe. The longitudinal distribution without magnetic field (Figure 8) shows a peak of power deposition located in the first 25 cm of the dipole length. The distribution is averaged on the X transverse direction from -5 to +5 cm, so the averaged values are not nil for -3.5<Y<3.5 cm.

Figure 9 and Figure 10 plot the difference of power deposition with and without the magnetic field. The presence of the magnetic field is inducing a decrease of the power deposition in the first centimetre around the beampipe (Figure 9) and in the 25 first centimetres longitudinally (Figure 10). The reduction can reach values up of 5 mW/cm^3.

4.4.4 Power deposition coming from the inner longitudinal and the front face surfaces

A front face and a longitudinal blackhole have been added to identify the contributions to the total power deposition in the dipole due to particles entering from different surfaces (
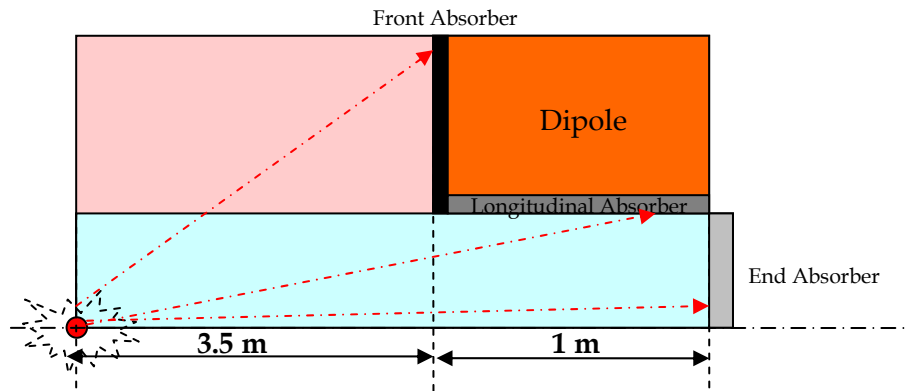
Figure 11).

Figure 11: FLUKA model with absorbers for detailed power distribution

Independent computations were performed, with the implementation of only one out of the 2 absorbers. The results in Table VI show that in this geometrical configuration (dipole at 3.5 m from the IP), the 2 contributions are almost equivalent, with a slightly larger value for the power deposition due to particles crossing the front face of the dipole. The statistical errors are evaluated on 5 runs of 2000 collisions and are below 5 %. The sum of the two contributions matches the total power deposition in the dipole of 74.7 W within the statistical fluctuations.

Power deposition	in the dipole	in the longitudinal absorber	in the front face absorber
Particles coming from the front face	37.9	119.6	0
Particles coming from the longitudinal inner surface	33.1	0	107.0

Table VI: Power deposition contribution from the front face and the longitudinal inner surfaces
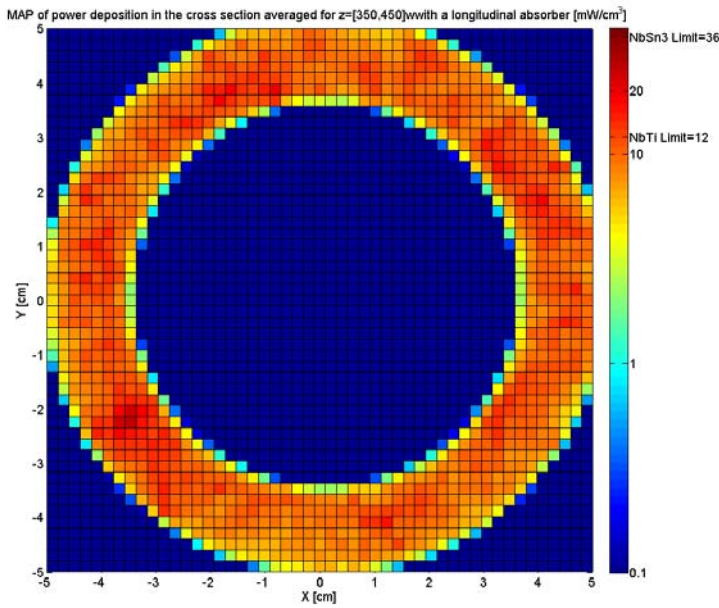
Figure 12: Radial distribution of power deposited from particles entering the dipole through the **front face surface.**
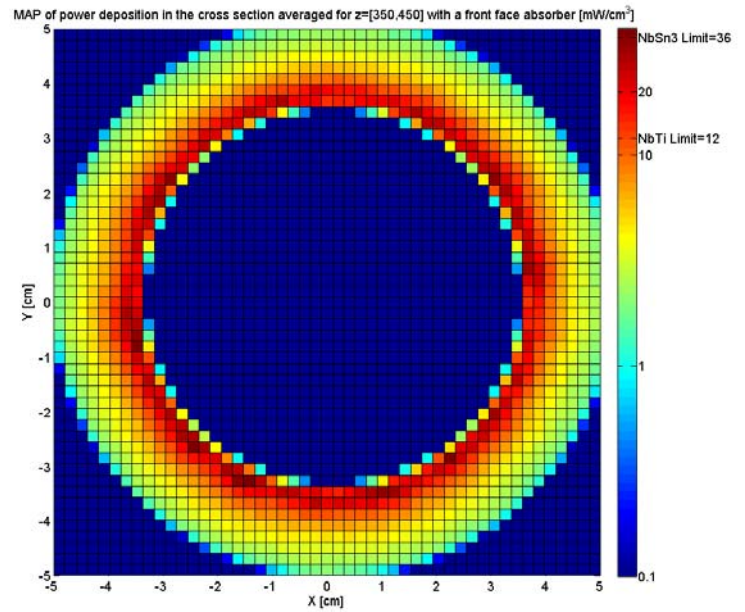

Figure 13: Radial distribution of power deposited from particles entering the dipole through the **longitudinal inner surfac**e
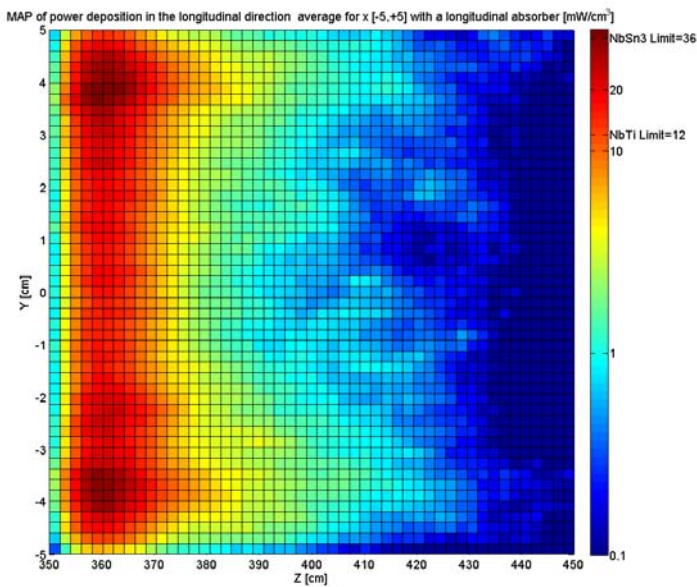

Figure 14: Longitudinal distribution of power deposited from particles entering the dipole through the **front face** surface, averaged on X [+5,-5] cm.
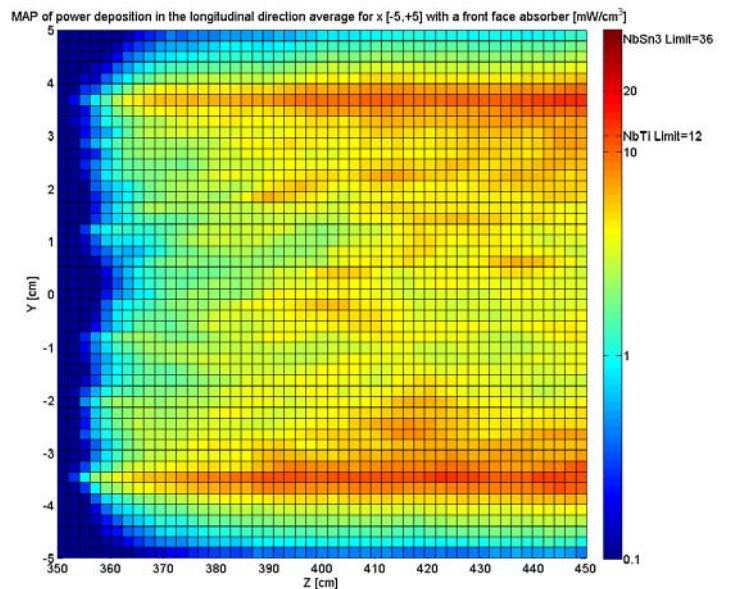

Figure 15: Longitudinal distribution of power deposited from particles entering the dipole through the **longitudinal inner surface**, averaged on X [+5,-5] cm.

Figure 12 and Figure 13 give the radial distribution of power deposition in the 2 configurations: The distribution is almost homogeneous for the particles entering through the front face (Figure 12) whereas, the particles entering through the beam pipe are deposing power in the inner layer of the dipole (Figure 13).

Figure 14 and Figure 15 give the longitudinal distributions of power deposition in the 2 configurations: the particles entering through the front face (Figure 14) deposit power in the first 25 cm of the dipole through electromagnetic cascades (see section 2.1.1). The power deposited by the particles entering through the longitudinal surface (Figure 15), is spreading all along the dipole, with a slightly increase at the end of the dipole. It is coherent with the increase of the pseudo-rapidity of the debris: the range of energy is higher for the particles hitting the end of the dipole.

4.5   Power deposition by different physical processes

In the FLUKA output file, the repartition of the total power is detailed by type of physical processes. Most of the total power of 18 kW escapes the system, so it means the particles are tracked until they are dumped in blackhole regions. The power deposition results mainly from electromagnetic cascade (more than 90%) and in small parts from hadron and muon ionisation, nuclear recoils and heavy ion fragmentation in the copper region. The discarded power is mostly due to neutrinos that are not tracked in our simulations. The missing energy is created out of nuclear binding energy balance: it is transformed into nucleus mass.

Detailed Power balance of FLUKA results	(W)	%
By hadron and muon ionisation	6.89	0.038
By electro magnetic cascade	69.99	0.388
By nuclear recoils and heavy ion fragmentation	0.10	0.001
By hadronic particle below threshold	0.00	0.00
Residual excitation energy	0.00	0.00
By low energy neutrons	0.02	0.00
Escaping the system	17935.84	99.550
Discarded	3.49	0.019
Out of the time limit	0.00	0.00
Missing energy (nuclear binding energy)	0.83	0.005
TOTAL treated by FLUKA	18016.94	100.00

Table VII: Power description for our FLUKA simulations

4.6 Power deposition by type of particles in D0

Different FLUKA runs have been performed to analyse the contribution of power deposition in D0 by particle family. The results presented in Table VIII could be compared to the impinging power evaluation found in [2]. The second and third columns of the table give respectively the repartition of the power deposition and the impinging power with respect to the particle families.

Only 36% of the impinging power is deposited inside the dipole. We can deduce the efficiency of the particle families in producing the heat deposition. The photons are the most important contributors with 19.4% of the total impinging power. In this category, we have summed up the secondary photons and the secondary pionzeros that decay in $\pi^0 \to 2\gamma$, just after the initial collision. The charged pions play also a big part of the power deposition with 10.1% of the total impinging power. The protons only contribute to 0.3% out of the 36.1% that is deposited in the dipole.

Particles	Power deposition 74.7 W	Impinging Power 209 W [2]
Photons (secondary photons+ pionzeros)	19.4% (2.6%+ 16.8%)	28.7 %
Charged pions	10.1%	45.1%
Neutrons	0.3%	2.2%
Protons	0.3%	2.4%
Electrons and positrons	0.05%	4.5%
Other particles	6.0%	17.0%
TOTAL	36.1%	100%

Table VIII: Power deposition in D0 by family of secondary particles

The longitudinal and radial distributions of power deposition are plotted for the 2 major contributors of the incoming particles: the photons (Figure 16, Figure 17) and the charged pions (Figure 18, Figure 19). Both contours show a peak power deposition at the entrance of the dipole. The difference in the power deposition distribution between the 2 particle families shows that the charged pions depose energy less efficiently than the photons: only 1/5 of the impinging charged pions depose power in the dipole, whereas 2/3 of the impinging photons contribute to power deposition.

It is consistent with the comparison of attenuation lengthes for these 2 particle families: for the example of 100 MeV particles (see Table I), the charged pions have attenuation length twice longer than the photons. The charged pions produce showers that are partially electromagnetic, and also hadronic with inelastic scattering interactions with the nuclei producing lower energy hadrons. The hadronic cascades penetrate more deeply inside the dipole.
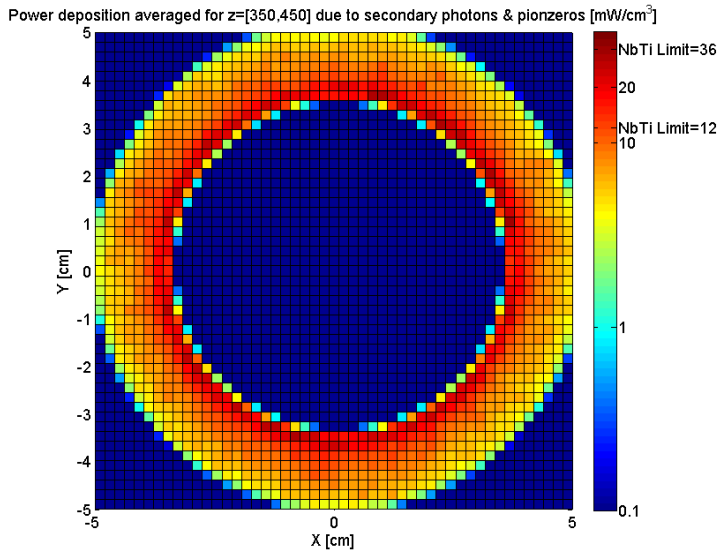
Power deposition averaged for z=[350,450] due to secondary photons & pionzeros [mW/cm³]

Power deposition average for x=[-5,+5] due to secondary photons & pionzeros [mW/cm³]

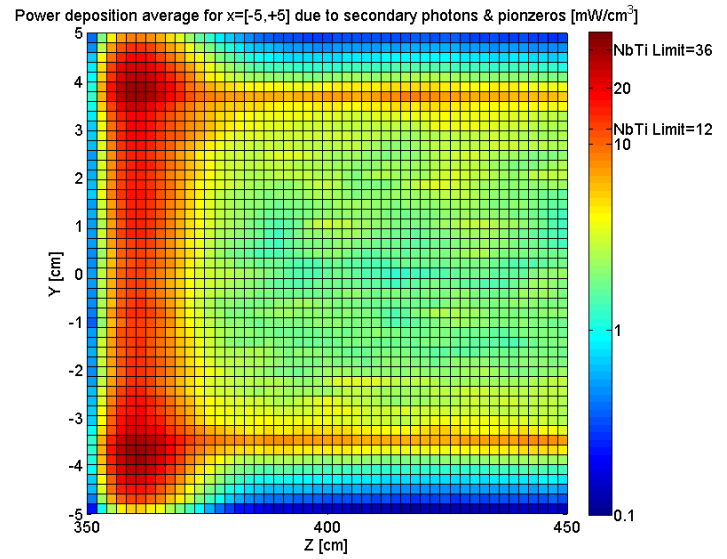Figure 16: Radial distribution of power deposited due to secondary photons and pionzeros.

Figure 17:Longitudinal distribution of power deposited due to secondary photons and pionzeros, averaged on X [+5,-5] cm.
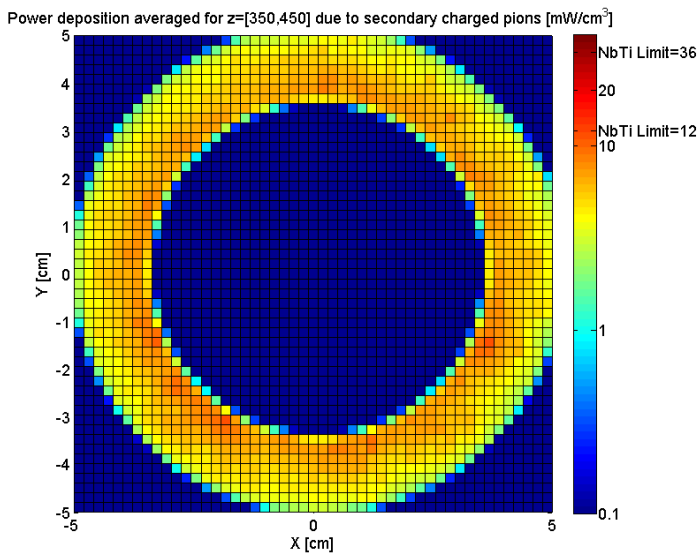
Power deposition averaged for z=[350,450] due to secondary charged pions [mW/cm³]

Power deposition averaged for x [-5,+5] due to secondary charged pions [mW/cm³]

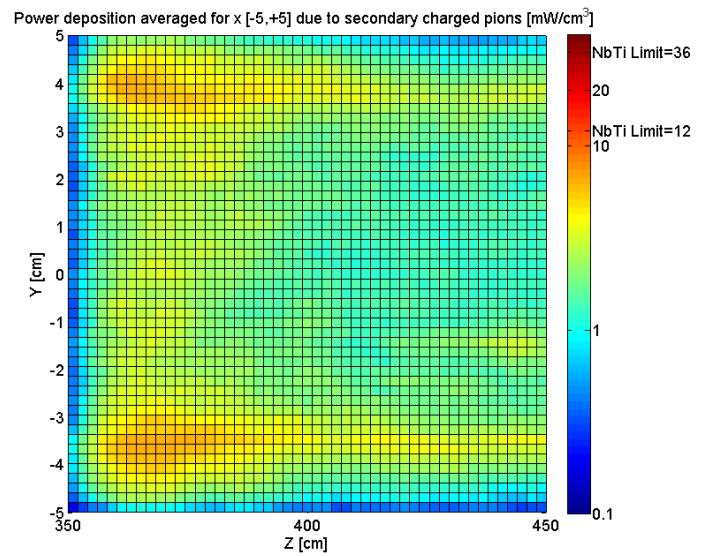Figure 18: Radial distribution of power deposited due to secondary charged pions.

Figure 19:Longitudinal distribution of power deposited due to secondary charged pions, averaged on X [+5,-5] cm.

5 Parametric studies on the dipole

5.1 Variation of power deposition with the distance from the IP

A parametric study has been performed with the simple model of the D0 dipole, located at different distances from the IP: 3.5, 9, 13 and 23 m. The results in Table IX and Figure 20, show that the power deposition increases when the dipole is farther away from the IP. This variation is in line with the increase of impinging energy with the distance to the IP analysed in [2]. This result is not intuitive, but is consistent with the energy spectra of secondaries that are travelling in the very forward direction: the most energetic particles have small polar angles with respect to the beam axis. With the dipole farther away from the IP, the opening of the cone on the dipole becomes narrower, corresponding to more energetic impinging particles.

Distance to the IP (m)	3.5	9	23
Power deposition in the D0 dipole (W)	74.7	110.9	145.6

Table IX: Parametric study on the distance from the IP

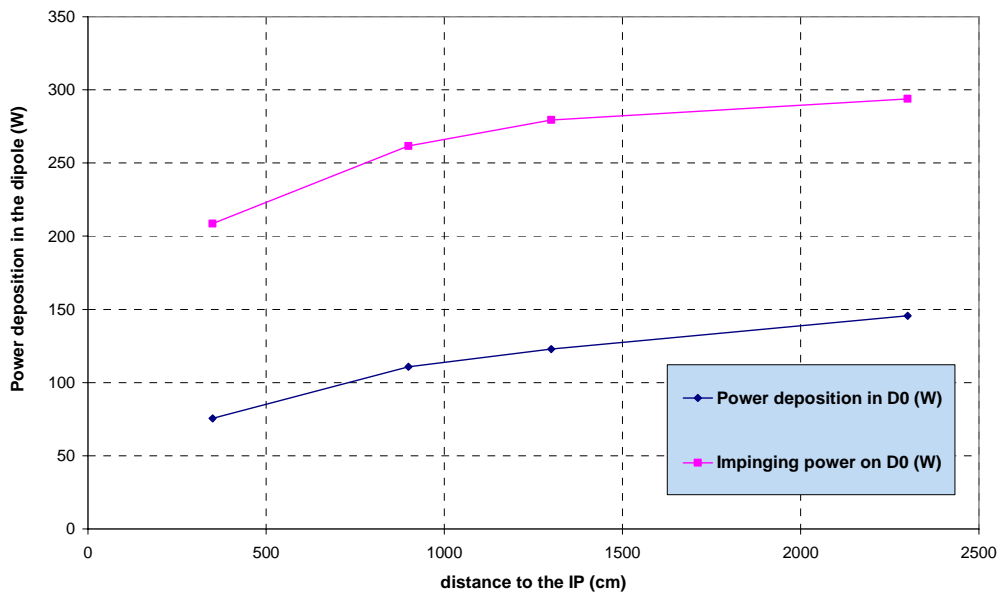Figure 20: Variation of Power deposition in D0 with the distance to the IP

5.2 Variation of power deposition with magnet aperture

The FLUKA model described in Figure 5 has been modified to investigate the influence of the magnet aperture diameter for a dipole at z=3.5 m. The aperture was increased from 70 mm to 110 mm. The 1.5 cm thickness for the dipole coil has been kept. The total power deposition in the dipole decreases from 74.7 W to 44.5 W. With an aperture of 110 mm, the secondary particles intercept the dipole region with a larger polar angle and therefore the energy spectra is shifted towards the lower energy ranges. The maximum peak heat density decreases more rapidly than the average and is reduced from 95 mW/cm^3 to 38 mW/cm^3. The power deposition distributions are shown in Figure 21 and Figure 22.

MAP of power deposition in the cross section averaged for z=[350,450] 110 mm aperture dipole [mW/cm³]

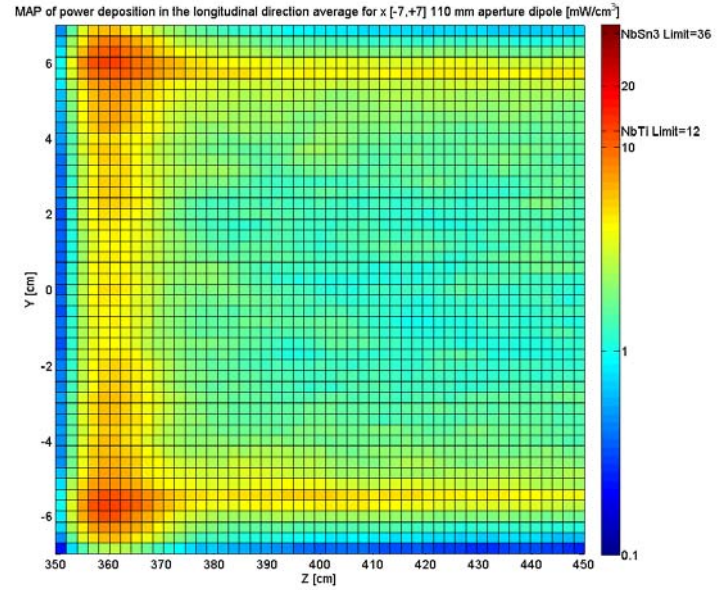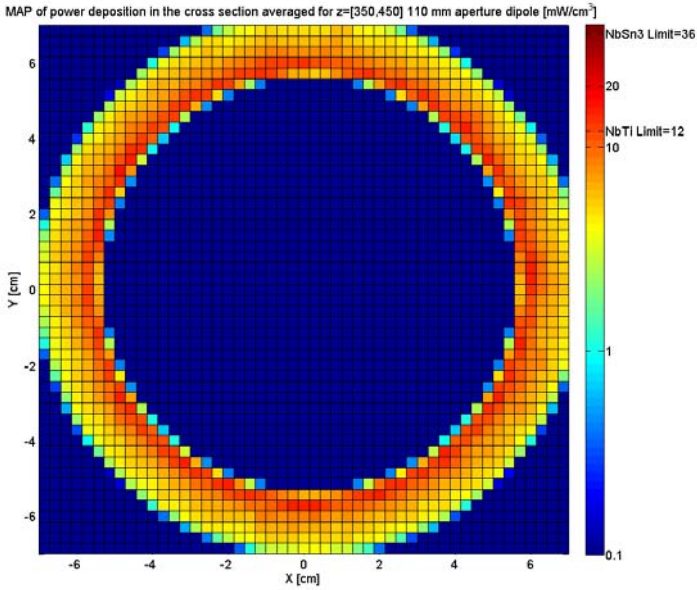MAP of power deposition in the longitudinal direction average for x [-7,+7] 110 mm aperture dipole [mW/cm³]

Figure 21: Radial distribution of power deposition with a 110 mm aperture dipole

Figure 22: Longitudinal distribution of power deposition with a 110 mm aperture dipole, averaged on X [+5,-5] cm.

6   Conclusion

These first results aim at giving some ideas of power deposition values for a D0 dipole in the experiment region, in an upgrade luminosity environment. To validate the FLUKA procedure, the energy deposited on the TAS was calculated and found in excellent agreement with results from other authors. A simplified model for both the D0 geometry and the collision has then been studied. The FLUKA computation has shown a high value of **74.7 W/m** for dynamic heat load, and heat density well above the quench levels of Nb-Ti or Nb$_3$Sn. Decreasing the heat deposition calls for shielding studies and adequate magnet design.

The variation with the magnetic field has not shown any great effect for the D0 proper. This first result should be further investigated with a more complete description of the bunch-bunch collisions and taking into account a crossing angle. The magnetic field of the experiment region should also be modelled as it can also have a non negligible impact on the tracking of the particles.

The contribution of the power deposition due the particles entering the different surfaces of the dipole have been detailed and the results show that, in the case of a dipole at 3.5 m from the IP, the total power deposition comes almost equally from the front face and longitudinal inner surfaces. Hence any shielding component should be designed to reduce both contributions.

The investigations have been focussed on the particle family that impinge and deposit power in the dipole. These particles are in the range of 1 to 10^3 GeV and are mostly photons (secondary photons and pionzeros that decay in $\pi^0 \rightarrow 2\gamma$ just after the collisions) and charged pions. The analyses revealed that more than 90% of the total power deposition is due to

electromagnetic showers induced by the photons and by the charged pions interacting with the matter.

Simple parametric studies have been performed to address the variations of power deposition with:

- a closer position of the dipole to the IP

- a larger aperture diameter for the dipole

These analyses open some paths to investigate in order to reduce power deposition to an acceptable level. Indeed both variations have shown to reduce the power deposition in the dipole. They both favour a geometry configuration where the dipole is swept by secondary particles with larger polar angles, and the energy spectra has shown that the particles are then less energetic, leading to a reduction of the total power deposited in the dipole. This first approach of a scaling law for energy power with respect to the distance to the IP is favourable to a dipole located in the experiment region. Hence these results of power deposition show a challenge, but a priori no critical showstoppers to the feasibility of an early separation dipole scheme from this point of view.

7   Acknowledgements

References

[1] 'Investigations of the parameter space for the LHC Luminosity Upgrade', J-P Koutchouk, EPAC, June 2006.

[2] 'Procedures and first investigation of the power radiated by proton-proton collisions into an early separation dipole for the LHC Luminosity Upgrade', C. HOA, LHC report

[3]: 'Beam induced energy deposition studies in IR magnets', N.V Mokhov, WAMDO workshop, Geneva, April 2006.

[4] 'Protecting LHC IP1/IP5 components against radiation resulting from colliding beam interactions', N.V Mokhov, I.L Rakhno, J.S. Kerby, J. B Strait, Fermilab, LHC report 633, April 2003.

[5] 'Study of the stability of the LHC low Beta inner triplet for a Nb_3Sn design', G. Ambrosio, F. Broggi, L. Rossi, INFN report INFN/ TC-99/04, March 1999.

[6] Particle Data Group, Chapter 27 'Passage of particles through matter', revised April 2006 by H. Bichsel, D.E Groom, and S.R Klein,

http://pdg.lbl.gov/2006/reviews/passagerpp.pdf

[7] Introduction to Nuclear and particle Physics, Chap 6 'Energy Deposition in media', Second edition, A. Das and T. Ferbel.

[8] Modern Physics, 4th Ed. W.H Freeman & Co., A. Tipler, A. Llewellyn, Chap 12: 'Interaction of Particles and Matter,

http://bcs.whfreeman.com/tiplermodernphysics4e/content/cat_020/InteractionParticlesandMatter.pdf

[9] Cours de l'Université de Genève, Chap7 'Interactions des particules avec la Matière'

http://dpnc.unige.ch/atlas/xin/noyaux/pdf2004/chapitre-7.pdf

[10] taken from L. Pages et al. (1972) Atomic Data, 4,1

http://www.kayelaby.npl.co.uk/atomic_and_nuclear_physics/4_5/4_5_1.html

http://www.kayelaby.npl.co.uk/atomic_and_nuclear_physics/4_5/4_5_2.html

[11] XCOM Photon cross sections databases, NIST Standard Reference Database 8 (XGAM) http://physics.nist.gov/cgi-bin/Xcom/xcom3_1

FLUKA licence references (version 2006.3):

[12] 'FLUKA: a multi-particle transport code', A. Fasso`, A. Ferrari, J. Ranft, and P.R. Sala, CERN-2005-10 (2005), INFN/TC_05/11, SLAC-R-773

[13] 'The physics models of FLUKA: status and recent developments',A. Fasso`, A. Ferrari, S. Roesler, P.R. Sala, G. Battistoni, F. Cerutti, E. Gadioli, M.V. Garzelli, F. Ballarini, A. Ottolenghi, A. Empl and J. Ranft, Computing in High Energy and Nuclear Physics 2003 Conference (CHEP2003), La Jolla, CA, USA, March 24-28, 2003, (paper MOMT005), eConf C0303241 (2003), arXiv:hep-ph/0306267